Kovove Mater. 64 2026 291–307
DOI: 10.31577/km.2026.5.291

Investigation on microstructure, Mn segregation behavior and mechanical properties of high-Mn steel joints

Wei Li[1,2], Kai Lu[1], Kun Liu[1]*, Jikui Shen[3], Guodong Wang[3], Wei Qin[3], Dayan Lu[3], Yue Ma[3], Jiasheng Zou[1], Tushar Sonar[4]

[1] *School of Materials Science and Engineering, Jiangsu University of Science and Technology, Zhenjiang, 212100, P. R. China*
[2] *Jiangsu Key Laboratory for Premium Steel Materials, Nanjing Iron & Steel Co., Ltd., Nanjing 210035, P. R. China*
[3] *Shandong Tengda Special Steel Wire Technology Co., Ltd., Tengzhou 277599, P. R. China*
[4] *Department of Welding Equipment and Technology, South Ural State University (National Research University), Chelyabinsk 454080, Russia*

Received 2 September 2026, received in revised form 2 October 2026, accepted 15 October 2026

Abstract

Shielded metal arc welding (SMAW) and submerged arc welding (SAW) were used to join 20 mm-thick 25Mn austenitic steel plates for cryogenic applications. The weld microstructure, Mn segregation, local stacking fault energy (SFE), and mechanical properties were compared. Both weld metals were predominantly γ-austenitic. SMAW produced finer columnar dendrites and higher geometrically necessary dislocation densities, whereas SAW produced coarser, more directionally aligned dendrites. Electron backscatter diffraction revealed more pronounced differences between the second and third SMAW layers than between the corresponding SAW layers. Interdendritic Mn enrichment occurred in both weld metals, with local segregation indices of approximately 12.5 % for SMAW and 33.8 % for SAW. Calculated SFE values were 24.0–30.5 mJ m^{-2} and 21.6–33.7 mJ m^{-2}, respectively, suggesting a tendency for twinning-induced plasticity. SMAW exhibited higher tensile strength and microhardness, whereas SAW showed greater elongation after fracture and higher absorbed impact energy at −196 °C. The mean weld-metal impact energies were 68 J and 91 J, respectively. These results link the differences in strength and ductility to microstructural refinement, dislocation substructures, and heterogeneity between and within weld layers.

K e y w o r d s: high-Mn austenitic steel, shielded metal arc welding, submerged arc welding, Mn segregation, cryogenic impact toughness

1. Introduction

With the growing global demand for clean energy in recent years, liquefied natural gas (LNG) has received considerable attention because of its high storage efficiency and low environmental impact [1–4]. LNG containment materials must retain adequate mechanical performance at cryogenic temperatures; testing at −196 °C is commonly used to evaluate their cryogenic toughness. Therefore, the materials used for LNG containment structures must possess not only high strength but also excellent cryogenic performance and acceptable economic efficiency [5, 6]. Conventional cryogenic alloys, such as 9Ni steel and Invar steel, exhibit excellent low-temperature properties [7–11]. However, their high Ni contents substantially increase material costs, thereby limiting their application in large-scale LNG storage tanks to some extent [12, 13]. Therefore, the development of alternative materials that combine excellent cryogenic performance with cost effectiveness is of considerable engineering significance [14, 15].

In recent years, high-Mn austenitic steel has been regarded as one of the most promising alternatives to 9Ni steel because it combines high strength, excellent cryogenic toughness, and favorable cost effec-

*Corresponding author: e-mail address: liu_kun@163.com

This article is distributed under the terms of the Creative Commons Attri-bution-NonCommercial 4.0 International Public License (CC BY-NC 4.0).

tiveness [16–19]. Previous studies have shown that the high Mn content expands the austenite stability region, enabling the steel to retain a stable austenitic microstructure even at cryogenic temperatures. Meanwhile, the plastic deformation behavior of high-Mn steel is closely associated with its stacking fault energy (SFE). The SFE affects the propensity for dislocation slip, mechanical twinning, and martensitic transformation, thereby influencing the strain-hardening capacity and the strength–toughness balance of the material [2, 12, 20–23]. An SFE range of approximately 20–40 $mJ\,m^{-2}$ is commonly associated with a tendency for twinning-induced plasticity (TWIP). This mechanism delays strain localization and improves ductility and toughness, giving high-Mn austenitic steels broad application prospects in the storage and transportation of cryogenic gases, including LNG [22].

In practical engineering applications, welding is an indispensable process in the fabrication of high-Mn steel structures, while the non-equilibrium thermal cycles introduced during welding may affect the above deformation mechanisms. Previous studies have shown that the microstructural morphology, solute segregation, and mechanical properties of high-Mn steel welded joints are jointly governed by the welding thermal cycle, filler-metal composition, and solidification conditions [3, 12, 20, 21]. During solidification, solute elements such as Mn are redistributed between dendrite cores and interdendritic regions, resulting in local solute-enriched and solute-depleted areas [24, 25]. As Mn is an important austenite-stabilizing element, variations in its spatial distribution may lead to local differences in SFE and subsequently affect the tendency for plastic deformation and the uniformity of properties across different weld-metal regions [26].

For multilayer multipass welds, individual weld layers experience different numbers and intensities of thermal cycles. The lower layers are repeatedly reheated during the deposition of subsequent passes, whereas the cap layer is subjected to relatively limited post-weld thermal cycling. This difference may alter the interdendritic morphology, crystallographic orientation, and elemental distribution among weld layers. Current studies on high-Mn steel welding have addressed welded-joint microstructures, tensile properties, cryogenic impact toughness, and solute segregation [1, 4, 17, 22, 27, 28]. However, the differences in Mn segregation within multilayer welds produced by different welding processes, as well as the relationship among local Mn distribution, SFE, and mechanical properties, require further investigation. In particular, macroscopic microstructural continuity across weld layers may coexist with dendrite-scale chemical heterogeneity; their combined effects on weld strength, microhardness, and cryogenic toughness have not yet been systematically compared.

Submerged arc welding (SAW) and shielded metal arc welding (SMAW) are currently among the most widely applied welding processes for high-Mn steel in engineering practice [29, 30]. Ren et al. [4] reported that high-Mn steel welds produced by SMAW exhibited a minimum cryogenic impact energy of 55 J. Jo et al. [31] employed SAW to weld 22Mn high-Mn steel and obtained a tensile strength of 789 MPa. Fan et al. [27] used Ni-based electrodes to weld high-Mn steel containing 24 wt.% Mn and found that the tensile properties of SMAW joints were superior to those of SAW joints. Under the conditions examined here, SAW used a higher heat input, whereas SMAW used a lower heat input associated with faster cooling and a finer weld microstructure. Variations in heat input, welding thermal cycles, and solidification conditions between these processes jointly affect dendrite growth and the redistribution of Mn between the solid and liquid phases, thereby influencing the weld microstructure and mechanical properties. Therefore, a comparative investigation of the relationships among weld microstructure, Mn segregation, and mechanical properties under these two practical welding processes can provide a reference for optimizing high-Mn steel welding procedures.

Accordingly, 25Mn high-Mn austenitic steel was selected in this study and welded using multilayer multipass SMAW and SAW. The weld microstructure, Mn segregation behavior, and mechanical properties under the two welding processes were systematically investigated. By combining local SFE calculations with microhardness, tensile, and cryogenic impact test results, the relationship between multiscale microstructural heterogeneity and the properties of the welded joints was further discussed.

2. Materials and methods

2.1. Materials

‘Q400GMDR steel plates with dimensions of 300 mm × 200 mm × 20 mm, manufactured by Nanjing Iron and Steel Group Co., Ltd., were used as the base metal (BM). The chemical composition and mechanical properties of the base metal are listed in Tables 1 and 2, respectively. The chemical compositions of the deposited weld metals are provided in Table 3.

To investigate the effects of different welding processes on the microstructural evolution and Mn segregation behavior of high-Mn steel, SMAW and SAW were employed, with the joint cross-sections shown in Fig. 1. All welded joints were prepared with an X-groove configuration, a single-side groove angle of 30°, a root-face height of 1.5–2.0 mm, and a root gap of approximately 3.9–4.0 mm. Before welding, the groove surfaces and the adjacent regions within ap-

Table 1. Chemical composition of the base metal (wt.%)

C	Si	Mn	P	S	Cr	Ni	Cu	Mo	B	Fe
0.35–0.55	0.1–0.5	22.5–25.5	≤ 0.03	≤ 0.01	3–4	≤ 0.05	0.3–0.7	≤ 0.3	≤ 0.005	Bal.

Table 2. Mechanical properties of the Q400GMDR high-Mn steel

Tensile strength (MPa)	Yield strength (MPa)	Elongation after fracture (%)
861	552	51

Table 3. Chemical compositions of the deposited weld metals (wt.%)

Element	C	Si	Mn	Ni	Cr	P	S	Fe
SMAW	0.25	0.35	23.54	4.31	2.37	0.007	0.002	69.171
SAW	0.32	0.45	22.18	3.3	3.1	0.021	0.03	70.599

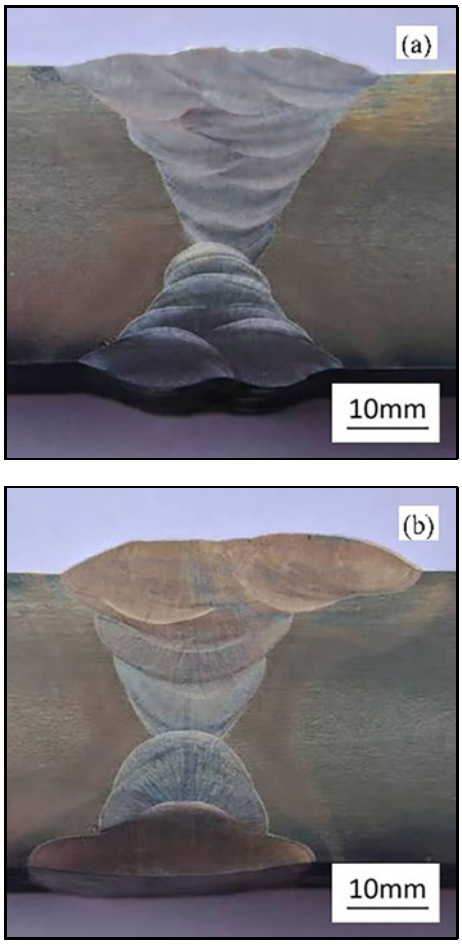


Fig. 1. Cross-sectional macrographs of the welded joints: (a) SAW, (b) SMAW.

proximately 20 mm on both sides were mechanically ground and cleaned with acetone to remove grease, oxide scale, and other surface contaminants, thereby ensuring weld quality. SMAW was performed using TMF25Mn electrodes at a welding current of 100 A and a voltage of 26–28 V, corresponding to a heat input of 9.5–10.5 kJ cm^{-1}. SAW was conducted using MCJGMn wire in combination with TMSJGMn flux at a welding current of 340–360 A, a voltage of 38–40 V, and a welding speed of 6.7 mm s^{-1}, corresponding to a heat input of 19.6–20.7 kJ cm^{-1}.

Based on the applied welding parameters, SAW involved a higher heat input, which is expected to produce a larger molten pool, a longer solidification time. These conditions promote dendrite growth and solute redistribution. In contrast, the lower heat input and faster cooling rate of SMAW favor the formation of a refined solidification microstructure. The two representative heat-input conditions were therefore used to investigate the effects of welding heat input on Mn segregation, microstructural evolution, and mechanical properties. It should be noted that the two experimental conditions also differed in welding process and consumable composition. Accordingly, the results discussed below reflect the combined effects of these two practical welding conditions.

2.2. Microstructural characterization

After welding, specimens were sectioned transverse to the welding direction, mechanically ground and polished, and then etched in a 10 vol.% nitric acid-ethanol solution for 60 s to reveal the weld microstructures. X-ray diffraction (XRD) was used to identify the phases in the base metal and the SMAW and SAW weld metals. Optical microscopy (OM) and scanning electron microscopy (SEM), combined with energy dispersive spectroscopy (EDS), were employed to examine the

microstructural evolution of the first to fourth weld layers under repeated welding thermal cycles, as well as the distribution characteristics of Mn.

To assess the possible influence of local composition on deformation behavior, the chemical compositions obtained by EDS were used in conjunction with *JMatPro software* to calculate the SFEs of Mn--enriched and Mn-depleted regions. These calculations were used to assess the potential deformation tendencies, rather than to establish the active deformation mechanisms directly. Electron backscatter diffraction (EBSD) was performed in the central regions of the second and third weld layers to characterize grain size, grain-boundary misorientation, and local orientation gradients. Inverse pole figure (IPF) maps, grain--boundary (GB) maps, and kernel average misorientation (KAM) maps were analyzed.

The second and third layers were selected because they are adjacent intermediate layers that permit a comparison of the microstructure after different subsequent reheating histories. The first layer experiences repeated reheating during deposition on both sides of the joint, whereas the fourth layer retains a cap-layer solidification structure without subsequent reheating. Focusing on the two intermediate layers reduces the influence of these distinct root and cap conditions on the comparison between SMAW and SAW. OM and SEM observations covered all four layers to establish the overall morphological trends.

Grain boundaries were classified by their misorientation angle θ: low-angle grain boundaries (LAGBs) corresponded to $2° \leq \theta \leq 15°$, and high-angle grain boundaries (HAGBs) to $\theta > 15°$. Misorientations below 2° were excluded from these boundary fractions. The same classification was used for the four EBSD regions.

2.3. Mechanical properties

Vickers microhardness tests were performed using a Vickers microhardness tester (HV0.2) under a load of 1.961 N with a dwell time of 20 s. Measurements were conducted along directions parallel and perpendicular to the welded joint to evaluate the relationship between microstructure and microhardness distribution. Room-temperature tensile tests were conducted using a universal testing machine in accordance with GB/T 228.1-2021. Cryogenic impact tests were performed at −196 ℃ using specimens extracted from the weld center, regions near the fusion line (FL), and the heat-affected zone (HAZ). The effects of Mn segregation and microstructural gradients on the cryogenic toughness of the welded joints were evaluated by comparing the absorbed impact energies of the different regions.

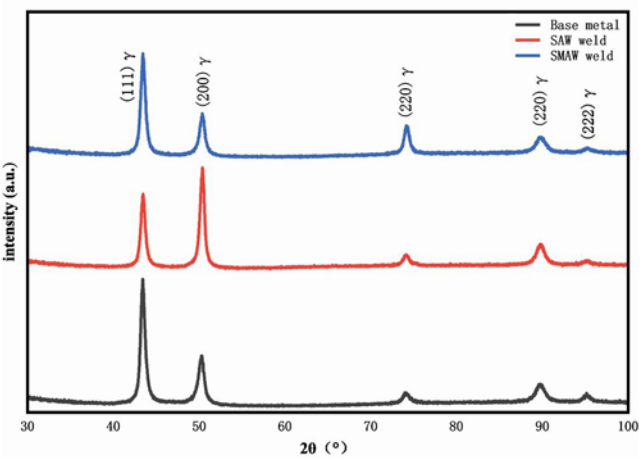


Fig. 2. XRD patterns of the BM, SAW weld metal, and SMAW weld metal of the high-Mn steel.

3. Results and analysis

3.1. XRD phase analysis

To clarify the effects of different welding processes on the phase constituents of high-Mn steel welds, XRD analysis was performed on the base metal (BM), SMAW weld metal, and SAW weld metal. The corresponding results are shown in Fig. 2.

Only characteristic diffraction peaks of γ-Fe were detected in the base metal and both weld metals, corresponding primarily to the (111), (200), (220), (311), and (222) crystal planes. No characteristic peaks of ε-martensite (ε-M) or $\alpha\prime$-martensite ($\alpha\prime$-M) were observed. These results indicate that the weld metals produced by both SMAW and SAW were predominantly austenitic.

The stable austenitic microstructure in high-Mn steel welds is mainly attributed to their high Mn content. As a typical austenite-stabilizing element, Mn significantly expands the stability range of the γ phase and decreases the driving force for $\gamma \rightarrow \varepsilon$ and $\gamma \rightarrow \alpha\prime$ transformations. Consequently, the weld metals remain predominantly austenitic despite rapid solidification and subsequent multilayer welding thermal cycles. These results indicate that the effects of the two welding processes are primarily reflected in solidification-microstructure characteristics, dendrite morphology, and the degree of elemental segregation, rather than in phase-constituent changes. Therefore, the differences in mechanical properties between the welds are discussed in terms of solidification behavior, Mn segregation, and microstructural heterogeneity under the two welding conditions.

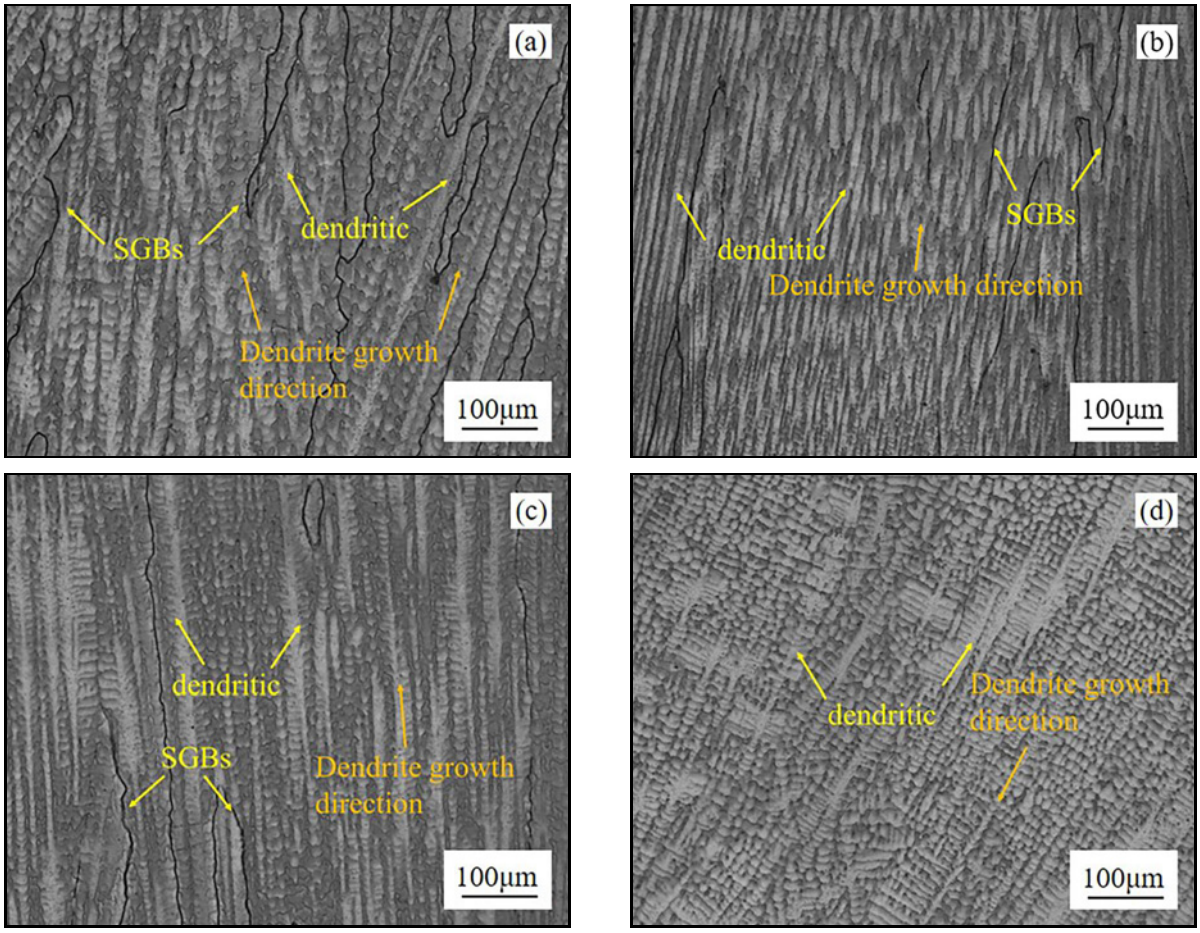


Fig. 3. Optical micrographs of the SMAW weld metal: (a) first layer, (b) second layer, (c) third layer, and (d) fourth layer.

3.2. Microstructural analysis of SMAW and SAW welds

3.2.1. Solidification microstructural characteristics of SMAW and SAW welds

Figures 3 and 4 show the microstructures of layers 1–4 in the SMAW and SAW welds, respectively. Both weld metals exhibit typical dendritic solidification morphologies. Combined with the XRD results, the matrix was confirmed to consist predominantly of columnar austenite grains. However, differences in heat input, molten-pool geometry, and cooling conditions between the two welding processes resulted in significant differences in columnar-grain size, dendrite growth direction, and interlayer microstructural morphology.

As shown in Figs. 3 and 4, both weld metals consist of directionally solidified columnar dendrites, although their dendrite size and growth orientation differ. The SMAW weld metal exhibits generally finer dendrites, and the dendrite boundaries are locally blunted as a result of repeated reheating. In contrast, the columnar dendrites in layers 1–4 of the SAW weld metal are overall coarser, show a more concentrated growth orientation, and exhibit more pronounced continuity in dendrite alignment.

These differences are mainly associated with the heat input and solidification conditions of the two processes. SMAW, with a heat input of 9.5–10.5 kJ cm^{-1}, produces a smaller molten pool and a faster cooling rate, which restrict dendrite growth and result in finer columnar grains. In contrast, SAW, with a heat input of 19.6–20.7 kJ cm^{-1}, is expected to maintain a higher molten-pool temperature and longer high-temperature residence and solidification times. These conditions provide more time for preferential growth of columnar dendrites, thereby resulting in a larger dendrite size.

From layers 1 to 4, the dendrite size in both weld metals exhibits interlayer variations rather than a strictly monotonic increase. As shown in Figs. 3a–d, the first SMAW layer was subjected to multiple subsequent thermal cycles, resulting in blunted dendrite contours and a non-uniform dendrite-size distribution. The dendrites in the second layer were relatively fine. Subsequently, with the progressive accumulation of welding heat, the dendrites in the third and fourth lay-

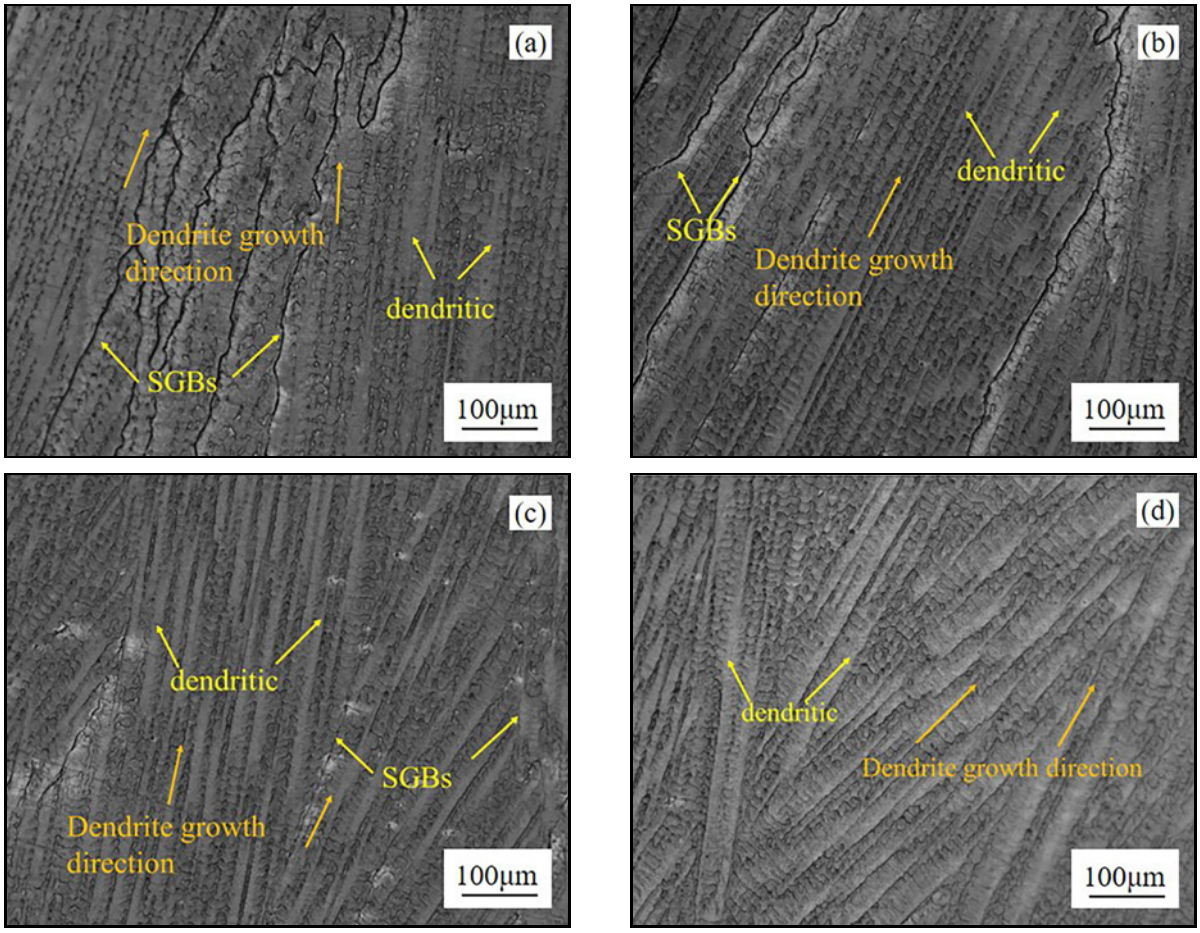


Fig. 4. Optical micrographs of the SAW weld metal: (a) first layer, (b) second layer, (c) third layer, and (d) fourth layer.

ers became generally more fully developed. As shown in Figs. 4a–d, the dendritic microstructure in all SAW layers was comparatively coarse. With increasing heat accumulation, the primary dendrite-arm size and dendrite spacing gradually increased from the second to the fourth layer. In particular, because the fourth layer was not reheated by subsequent weld passes, it retained a relatively complete, coarse, and regularly aligned as-solidified morphology.

The microstructural analysis indicates that welding heat input and cooling rate govern the overall scale and directionality of the solidification microstructures in the two weld metals. SMAW is characterized by relatively refined dendrites with more dispersed growth orientations, whereas SAW is dominated by coarse columnar dendrites with continuous directional growth. Furthermore, multilayer welding thermal cycles affect microstructural uniformity within each weld metal: SMAW exhibits more pronounced variations in dendrite size among the four layers, whereas SAW retains stronger continuity of the columnar dendritic structure overall.

3.2.2. EBSD analysis of the second and third weld layers in SMAW and SAW welds

To further evaluate the effects of welding thermal cycles on crystallographic orientation and grain-boundary characteristics, EBSD measurements were conducted in the central regions of the second and third weld layers produced by SMAW and SAW. Figure 5 presents the IPF maps and grain-size distribution histograms for these regions. All four weld regions exhibit columnar austenite grains elongated along the solidification direction. Clear color differences are observed between grains with different orientations, while continuous color gradients are present within some columnar grains, indicating a certain degree of local orientation variation within the grains.

The grain sizes in the analyzed regions were statistically evaluated. The average grain sizes of the second and third SMAW layers were 124.74 and 144.29 μm, respectively, whereas those of the corresponding SAW layers were 151.33 and 153.92 μm, respectively. For the same weld layer, the average grain size of the SMAW weld metal was consistently smaller than that of the

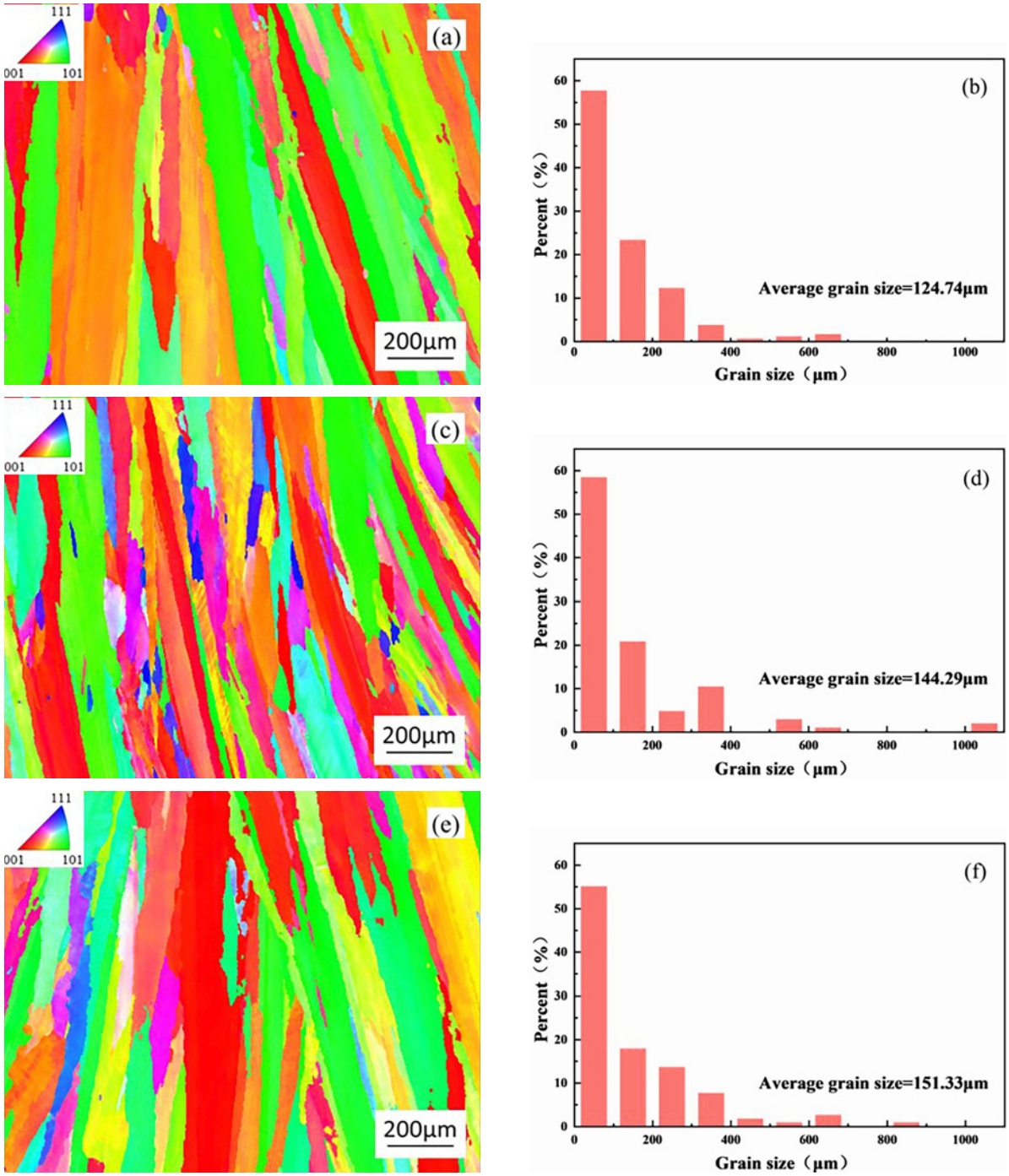


Fig. 5. IPF maps and grain size distribution maps of the second and third weld layers:(a), (b) SMAW-L2; (c), (d) SMAW--L3; (e), (f) SAW-L2; (g), (h) SAW-L3.

SAW weld metal, in agreement with the overall metallographic observation that SMAW produced a relatively refined microstructure whereas SAW produced a comparatively coarse microstructure. For the same welding process, the average grain size increased by approximately 15.7 % from the second to the third layer in SMAW, but by only approximately 1.7 % in SAW. These results indicate a more pronounced grain-size variation between the second and third SMAW layers, whereas the average grain sizes of the two SAW layers were more similar, consistent with the metallographic observations.

Figure 6 presents the KAM maps of the second and third weld layers produced by SMAW and SAW. The estimated geometrically necessary dislocation (GND) densities of the second and third SMAW layers were 0.45×10^{14} and 0.26×10^{14} m^{-2}, respectively, corresponding to a decrease of approximately 42.2 % from

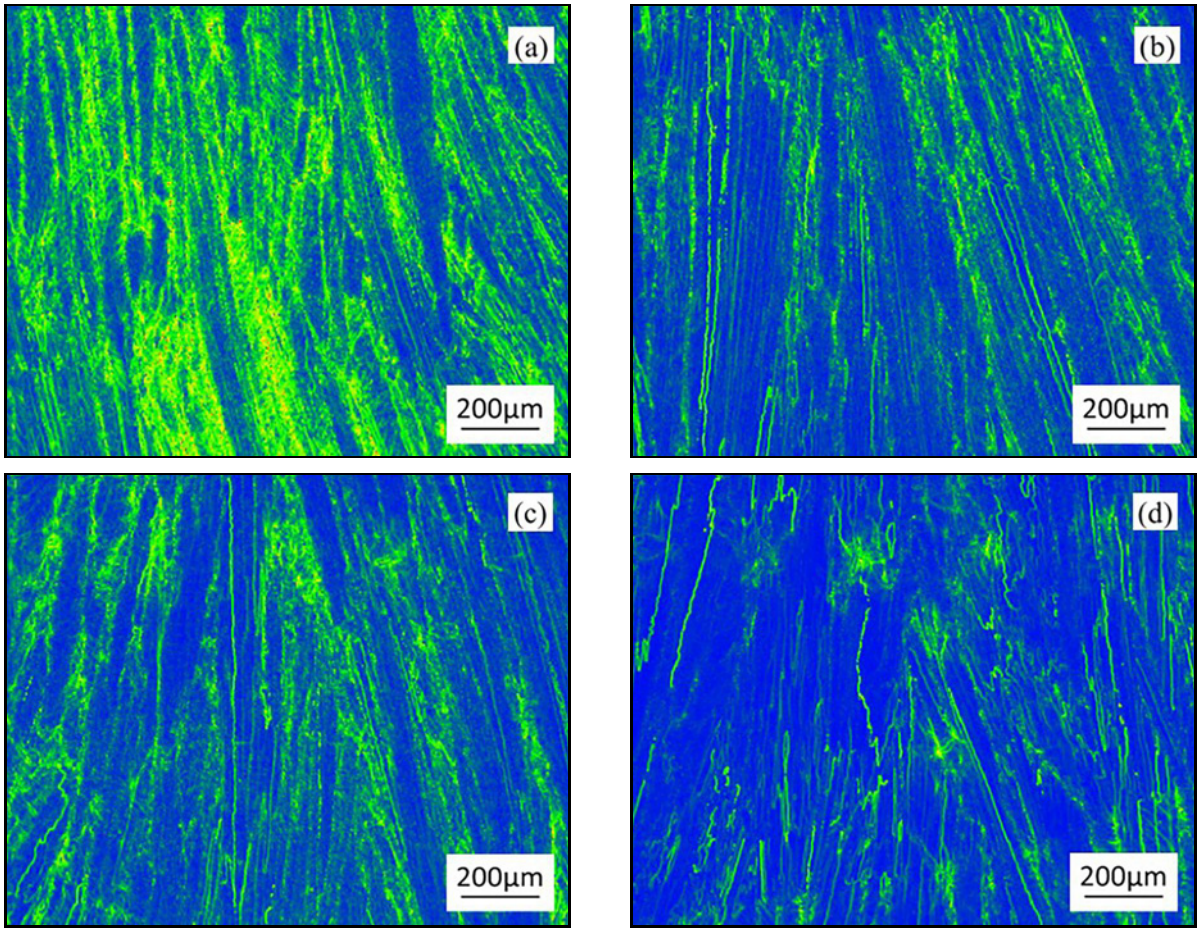


Fig. 6. KAM maps of the second and third weld layers for SMAW and SAW: (a) SMAW-L2, (b) SMAW-L3, (c) SAW-L2, and (d) SAW-L3.

the second to the third layer. The corresponding values for SAW were 0.28×10^{14} and 0.19×10^{14} m^{-2}, respectively, representing a decrease of approximately 32.1 %. For the same weld layer, SMAW consistently exhibited a higher GND density than SAW, indicating larger local lattice-orientation gradients and more pronounced substructural characteristics in the SMAW weld metal. This behavior is associated with the faster cooling rate, larger local temperature gradient, and incomplete relaxation of thermal strain during multilayer SMAW. For both welding processes, the GND density in the second layer was higher than that in the third layer, indicating that the lower weld layer developed a more complex local orientation state under the influence of subsequent weld passes. Because the second layer experienced more intense subsequent thermal cycling and greater constraint from the surrounding material, accumulated thermal strain and local dislocation rearrangement jointly produced higher orientation gradients. In contrast, the third layer experienced fewer subsequent thermal cycles and lower constraint; consequently, its GND density decreased.

Figure 7 shows the grain-boundary distributions of the different weld layers. In the second SMAW layer, the fraction of LAGBs reached 66.4 %, substantially exceeding that of HAGBs (33.6 %). In the third SMAW layer, the LAGB fraction decreased to 46.2 %, whereas the HAGB fraction increased to 53.8 %, corresponding to an interlayer change of 20.2 percentage points. The higher LAGB fraction in the second SMAW layer is consistent with its higher GND density, indicating the presence of more subgrain boundaries and low-angle boundaries associated with local orientation gradients. In contrast, the LAGB fractions in the second and third SAW layers were 44.6 and 43.9 %, respectively, while the corresponding HAGB fractions were 55.4 and 56.1 %. The interlayer difference was only 0.7 percentage points. Both SAW layers were dominated by HAGBs and exhibited more similar grain-boundary misorientation characteristics.

3.2.3. Comparative analysis of the microstructures of SMAW and SAW welds

The combined OM and EBSD results indicate that both weld metals exhibit solidification microstructures dominated by columnar austenite; however, substantial microstructural differences arise from their dis-

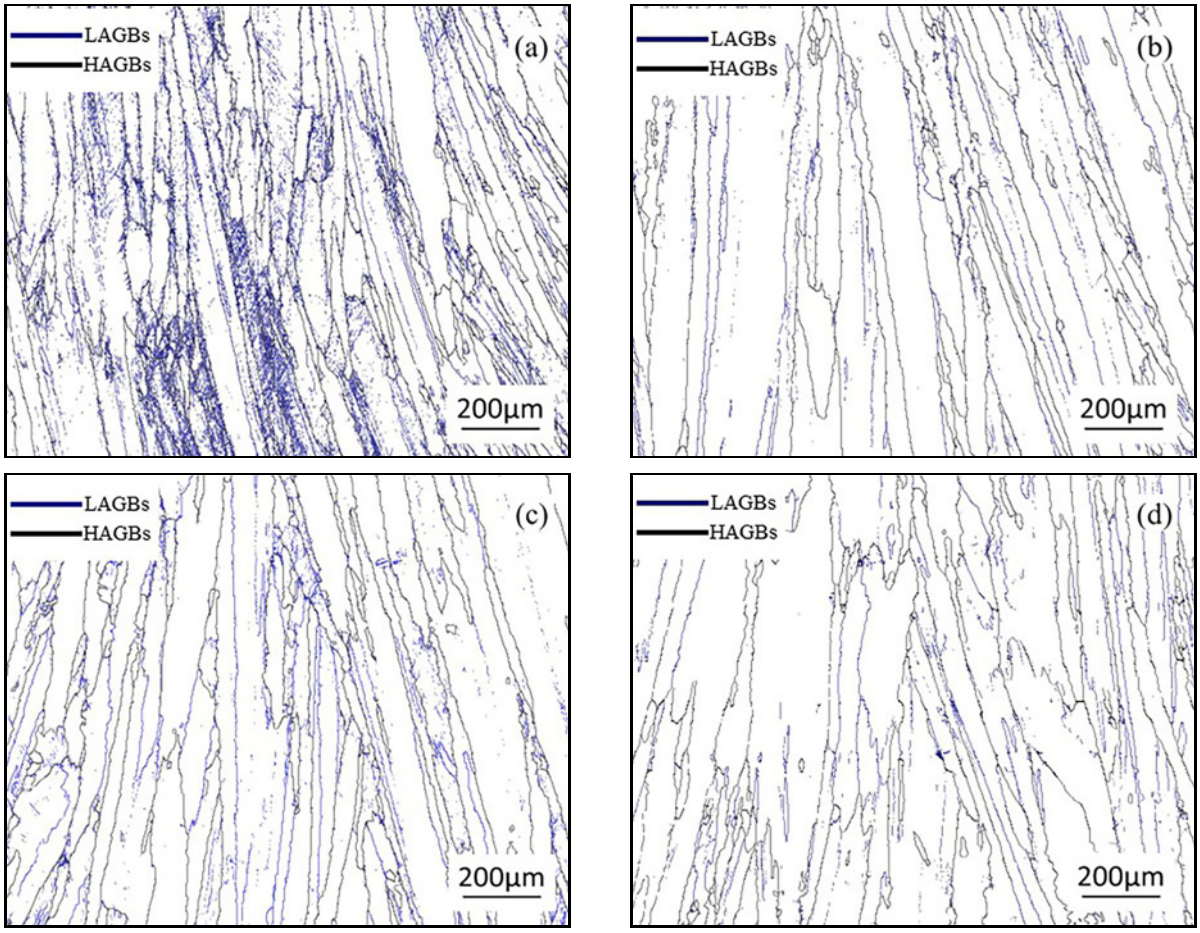


Fig. 7. GB maps of the second and third weld layers for SMAW and SAW: (a) SMAW-L2, (b) SMAW-L3, (c) SAW-L2, and (d) SAW-L3.

tinct welding processes and heat inputs. The faster cooling rate during SMAW restricts the growth of dendrites and austenite grains, resulting in average grain sizes of 124.74 μm and 144.29 μm in the second and third layers, respectively. In contrast, the longer high-temperature residence time of the molten pool and the longer solidification time during SAW promote columnar-grain growth, yielding corresponding average grain sizes of 151.33 μm and 153.92 μm and a more closely aligned growth orientations.

Multilayer welding thermal cycles further produced interlayer variations in crystallographic characteristics. Between the second and third SMAW layers, the average grain size differed by approximately 15.7 %, the GND density decreased by 42.2 %, and the LAGB fraction differed by 20.2 percentage points. These results indicate pronounced differences in grain size, intragranular orientation gradients, and grain-boundarys distribution between the two SMAW layers. In contrast, the average grain size and LAGB fraction of the second and third SAW layers differed by only approximately 1.7 % and 0.7 percentage points, respectively, indicating more similar grain size and grain-boundarys misorientation distributions. Nevertheless, the GND density still decreased by 32.1 %, demonstrating, that the interlayer microstructure of the SAW weld was not completely uniform.

In summary, SMAW is characterized by relatively refined dendrites and austenite grains, higher local orientation gradients, and more pronounced interlayer variations. In contrast, SAW exhibits coarser columnar grains, more fully developed directional growth, lower GND density, and more similar grain sizes and grain-boundary characteristics between the second and third layers.

3.3. Mn segregation and distribution under different welding processes

3.3.1. Dendrite-scale elemental distribution characteristics

To characterize Mn segregation at the dendrite scale, EDS line scans were performed across representative dendrites in the two weld metals. The line-scan profiles are shown in Fig. 8.

Mn exhibited a distinct alternating enrichment-depletion distribution along the scanning path. The

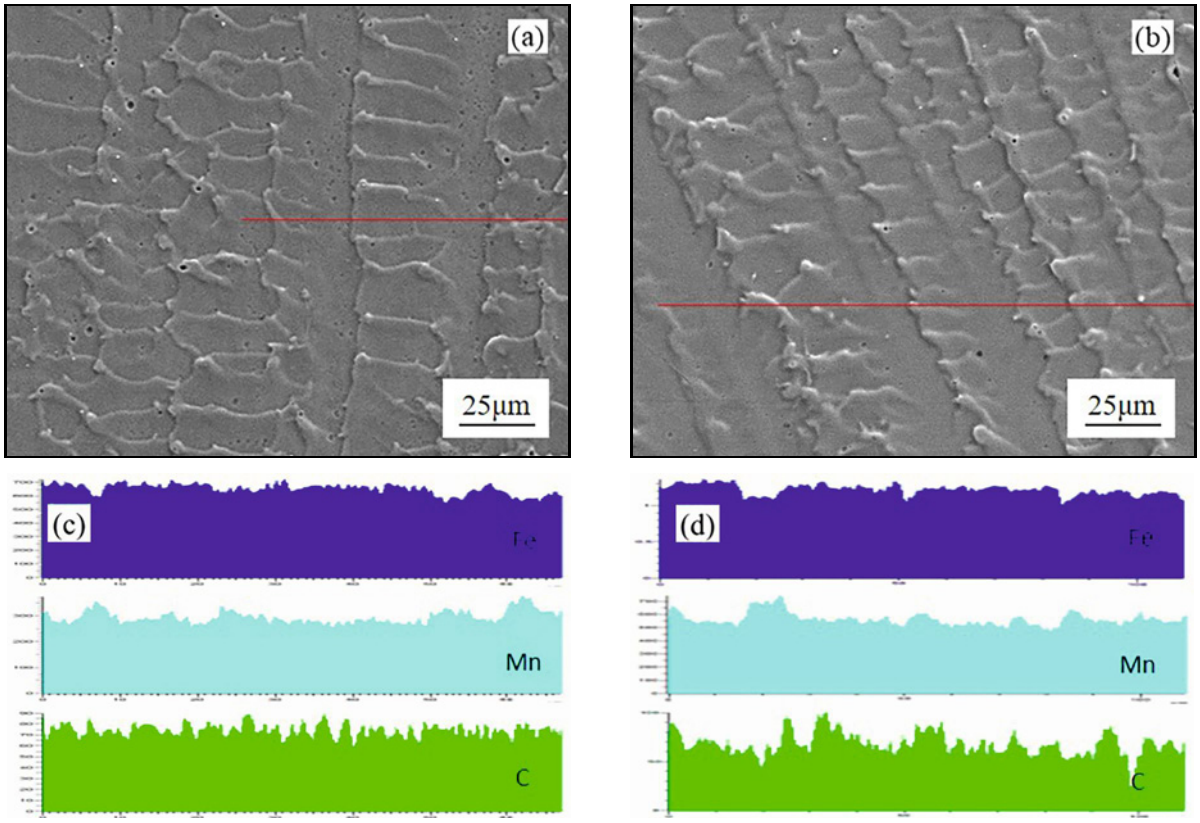


Fig. 8. EDS line scan maps and element distribution profiles for dendritic regions of SMAW and SAW weld metals.

Mn peaks were mainly located in the interdendritic regions, whereas the valleys were primarily located within the dendrites. Meanwhile, Fe showed the opposite trend: Mn-enriched regions corresponded to lower Fe contents, whereas Mn-depleted regions exhibited relatively higher Fe contents. This result indicates an evident complementary partitioning behavior between Mn and Fe during solidification. Such a distribution is consistent with the metallurgical principle that the Mn partition coefficient is lower than unity ($k_{\mathrm{Mn}} < 1$) during the solidification of high-Mn steel [22]. Mn is continuously rejected into the remaining liquid ahead of the solidification front, causing progressive Mn enrichment in the interdendritic liquid and relative Mn depletion within the dendrites.

A further comparison of the two welding processes revealed that the fluctuation amplitude of Mn in the SAW weld metal was markedly greater than that in the SMAW weld metal, indicating more pronounced Mn segregation under the higher-heat-input SAW condition. This behavior is mainly attributed to the larger molten pool and longer solidification time in SAW, which provide more time for Mn diffusion into the interdendritic liquid.

3.3.2. EDS point analysis of dendritic regions

To further investigate the local compositional characteristics of the two weld metals, EDS point analyses were performed on regions with different contrast in the SEM micrographs, as shown in Fig. 9. For the SMAW weld metal, two representative locations were selected: an interdendritic region (Point 1) and a dendrite-core region (Point 2). For the SAW weld metal, three representative locations were selected: an interdendritic region (Point 1) and two dendrite-core regions (Points 2 and 3). The elemental compositions are listed in Table 4.

The EDS point-analysis results show clear differences in Mn content among the analyzed locations. The Mn content in the interdendritic regions was higher than that in the dendrite-core regions, whereas Fe exhibited the opposite trend. These results further confirm interdendritic Mn enrichment in both weld metals.

To quantitatively evaluate the degree of Mn segregation under different welding processes, a Mn segregation index (SI) was introduced:

$$\mathrm{SI} = (C_{\mathrm{Mn,max}} - C_{\mathrm{Mn,min}})/C_{\mathrm{Mn,average}}. \qquad (1)$$

Based on the Mn contents measured at Points 1 and 2 in the SMAW weld metal and at Points 1 and 3 in the SAW weld metal, the segregation indices were approximately 12.54 % for SMAW and 33.80 % for SAW. In addition, the Mn content in the inter-

Table 4. Elemental compositions (wt.%) of the EDS point analysis regions in the SMAW and SAW welds

	SMAW		SAW		
	Point 1	Point 2	Point 1	Point 2	Point 3
Mn	23.39	20.63	28.74	20.53	20.43
Fe	68.46	71.89	64.1	73.86	74.04

Table 5. Calculated SFE values of different regions in SMAW and SAW weld metals

Welding process	Point	Mn (wt.%)	SFE (mJ m^{-2})	Predicted deformation tendency
SMAW	1	23.39	30.5	TWIP
SMAW	2	20.63	24	TWIP
SAW	1	28.74	33.7	TWIP
SAW	2	20.53	21.6	TWIP
SAW	3	20.43	21.6	TWIP

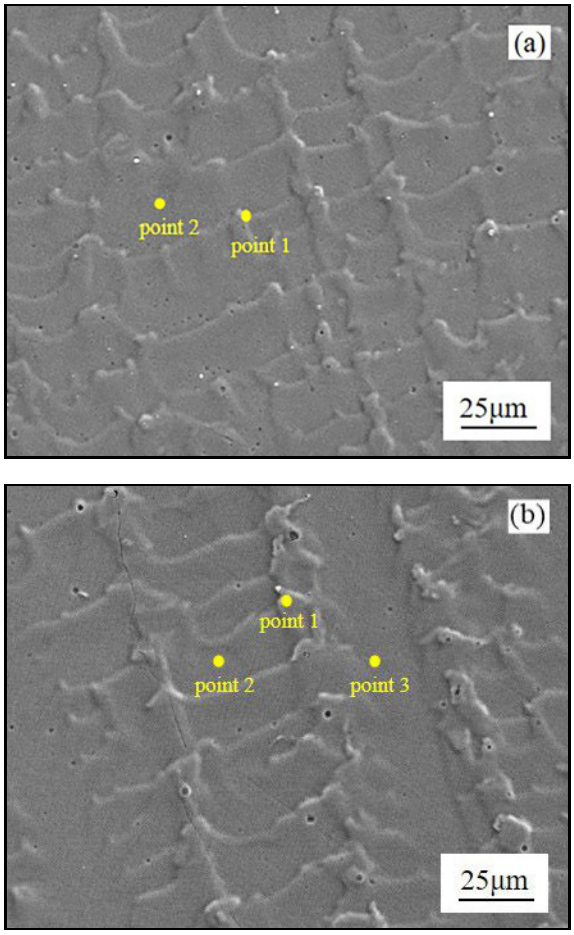


Fig. 9. Locations of EDS point analyses in the SMAW and SAW welds: (a) SMAW and (b) SAW.

dendritic region of the SAW weld metal (28.74 wt.%) was substantially higher than that in the corresponding SMAW region (23.39 wt.%). These results are consistent with greater solute redistribution into the remaining interdendritic liquid under the higher-heat-input SAW condition. In contrast, the rapid solidification during SMAW restricted the Mn diffusion distance, thereby producing Mn segregation at a relatively smaller scale.

3.4. Local stacking fault energy variations induced by Mn segregation

The excellent cryogenic ductility and toughness of high-Mn austenitic steels mainly originate from their stable austenitic matrix and the TWIP effect activated during deformation. In general, a relatively low SFE favors stacking-fault extension and ε-martensite formation, an intermediate SFE range promotes mechanical twinning, and a higher SFE tends to favor dislocation slip. However, the specific critical SFE values vary with chemical composition, temperature, grain size, and strain state [32–34]. Based on the EDS results, the local SFEs of different regions were calculated using *JMatPro software*, and the results are listed in Table 5. The SFE values of the weld-metal regions produced by the two welding processes ranged from 21.6 to 33.7 mJ m^{-2}, suggesting a tendency for TWIP in the analyzed weld-metal regions. Notably, Mn segregation produced clear local SFE variations within the weld metals. In the SAW weld metal, the SFE of the Mn-enriched region containing 28.74 wt.% Mn reached 33.7 mJ m^{-2}, whereas that of the Mn-depleted region containing approximately 20.5 wt.% Mn decreased to 21.6 mJ m^{-2}. The resulting SFE difference of approximately 12.1 mJ m^{-2} was substantially greater than that of the SMAW weld metal (6.5 mJ m^{-2}). These results indicate that the higher heat input promoted Mn redistribution during solidification, intensified dendrite-scale chemical segregation, and was associated with a larger local SFE variation.

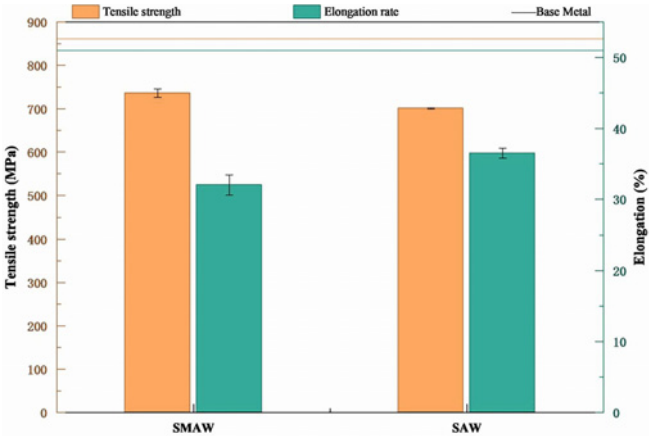


Fig. 10. Room-temperature tensile properties of the SMAW and SAW welded joints.

These results indicate that local SFE heterogeneity was greater in the SAW weld metal, whereas the SFE value in the SMAW weld metal was relatively concentrated. Under the higher-heat-input condition, the slower solidification process prolonged the coexistence of the liquid and solid phases, providing more favorable kinetic conditions for Mn migration into the remaining liquid. This promoted interdendritic Mn enrichment and generated more pronounced local chemical-composition and SFE variations. The calculated SFE values of all analyzed regions fell within a rang commonly associated with TWIP, suggesting that local compositional variations may alter the ease of stacking-fault formation and twinning. Therefore, within the same weld layer, a larger FE variationt may cause variations in deformation resistance among different regions of the SAW weld metal.

3.5. Mechanical properties and strengthening mechanisms

3.5.1. Tensile properties analysis

Figure 10 presents the room-temperature tensile properties of the SMAW and SAW welded joints. Both joints exhibited lower ultimate tensile strength and elongation after fracture than the base metal, whose corresponding values were 861 MPa and 51 % (Table 2). SMAW exhibited a higher ultimate tensile strength, whereas SAW achieved greater elongation after fracture, indicating different strength–ductility balances for the two welding processes.

The lower tensile properties of the joints can be associated with changes in microstructure and chemical composition during welding. Fusion and resolidification replace the original base-metal microstructure with a columnar dendritic structure, while subsequent thermal cycles can modify grain size and dislocation substructures. Such changes can alter grain-boundary strengthening and strain-hardening capacity [4, 14]. Composition is another factor: the deposited weld metals contain 0.25 wt.% C for SMAW and 0.32 wt.% C for SAW (Table 3), below the base-metal range of 0.35–0.55 wt.% (Table 1), which may reduce the contribution of interstitial solid-solution strengthening. In addition, the observed Mn segregation and interlayer microstructural differences can produce spatial variations in deformation resistance. Preferential strain accumulation in locally weaker regions may then limit the joint tensile strength and elongation. The retained γ-austenitic phase therefore does not imply tensile properties identical to those of the base metal.

Combined with the preceding microstructural analysis, the lower heat input and faster solidification rate of SMAW produced a relatively refined dendritic microstructure. In addition, the GND densities of the SMAW weld layers were consistently higher than those of the corresponding SAW layers. The higher GND density and LAGB fraction indicate more developed dislocation substructures and local orientation gradients within the weld metal. These can increase the resistance to subsequent dislocation motion, and thus contribute to the higher tensile strength of the SMAW joint. However, multilayer thermal cycling reduced microstructural uniformity. The substantial changes in grain-boundary characteristics and GND density between the second and third SMAW layers indicate possible differences in local deformation resistance among weld layers; consequently, its ductility was slightly lower than that of the SAW weld joint.

In contrast, SAW produced coarser columnar dendrites but more similar grain sizes and grain-boundary fractions between the second and third layers. Together with the lower GND densities, these features may facilitate strain accommodation between the analyzed layers. This similarity at the layer scale coexists with greater dendrite-scale Mn segregation and SFE variations. The calculated SFE values suggest a tendency for TWIP in the analyzed regions, but do not establish a uniform strain distribution during tensile loading. The greater elongation of the SAW joint is therefore consistent with its lower local orientation gradients and smaller differences between the two intermediate layers, although the contribution of each feature remains to be quantified.

In summary, SMAW achieved higher strength through its finer grains and higher GND density, whereas SAW exhibited greater ductility, consistent with its lower local orientation gradients and more stable interlayer grain-boundary characteristics. The differences in tensile properties result from the combined effects of microstructure, dislocation substructures, interlayer crystallographic similarity, and local chemical composition.

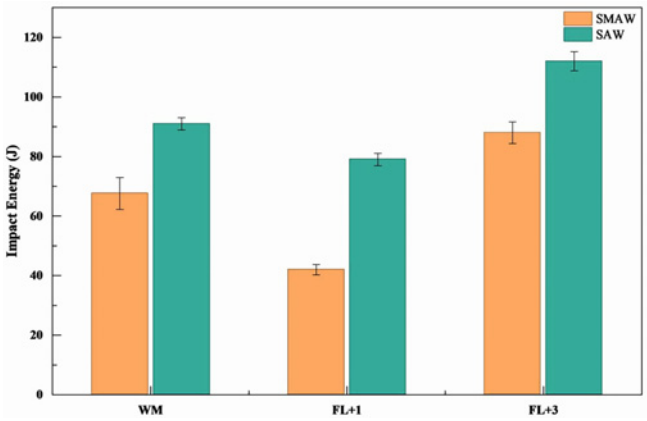


Fig. 11. Absorbed impact energies of the SMAW and SAW welded joints at –196 ℃.

3.5.2. Cryogenic impact properties at –196 °C

The cryogenic impact test results are presented in Fig. 11. Welded joints produced by both welding processes retained high absorbed impact energies, indicating that the 25Mn high-Mn steel weld metals maintained good cryogenic toughness at –196 ℃. However, variations in absorbed impact energy were observed among the different test locations for the two welding processes, demonstrating that welding thermal cycles exert an important influence on the cryogenic fracture behavior of the welded joints.

Overall, the absorbed impact energies of SAW were higher than those of SMAW at all test locations, with the average value at the weld center increasing from 68 to 91 J. Both weld metals were predominantly austenitic before testing, and their calculated local SFE values suggest a tendency for TWIP. Differences in the capacity to accommodate plastic deformation during crack propagation may therefore contribute to the impact-energy difference. The finer grains and higher GND density of SMAW are beneficial for strength; however, the relatively large variations in grain size, GND density, and grain-boundary characteristics between its second and third layers may generate more pronounced differences in interlayer deformation resistance. Although SAW exhibited coarser grains and greater local Mn/SFE fluctuations, its second and third layers showed more similar average grain sizes and grain-boundary fractions, together with lower GND densities.

3.5.3. Microhardness variation and strengthening mechanisms

Figure 12 presents the microhardness distributions across different weld layers in the SMAW and SAW welds. Figure 13 compares the overall microhardness variation of the two welding processes along

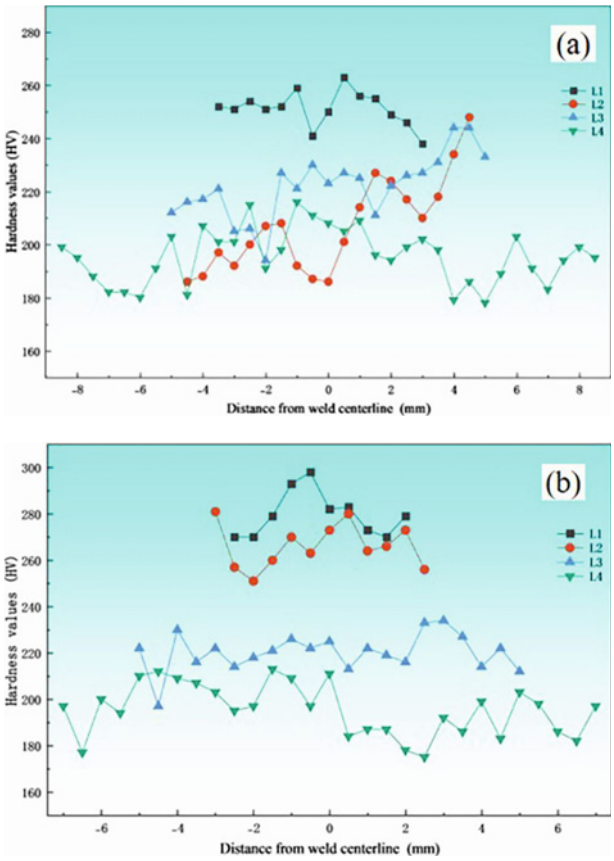


Fig. 12. Microhardness distribution maps of the weld regions: (a) SAW and (b) SMAW.

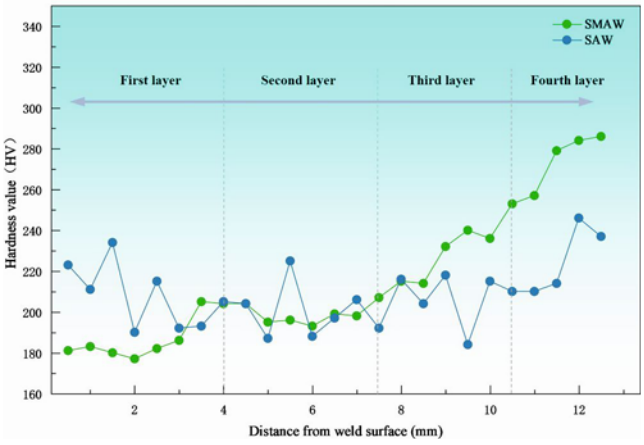


Fig. 13. Through-thickness microhardness profiles of the SMAW and SAW welded joints.

the transverse weld cross-section, while Fig. 14 compares the average microhardness values of the different weld layers. The two welding processes exhibited markedly different microhardness-distribution characteristics. The overall microhardness of the SMAW weld metal was higher than that of the SAW weld

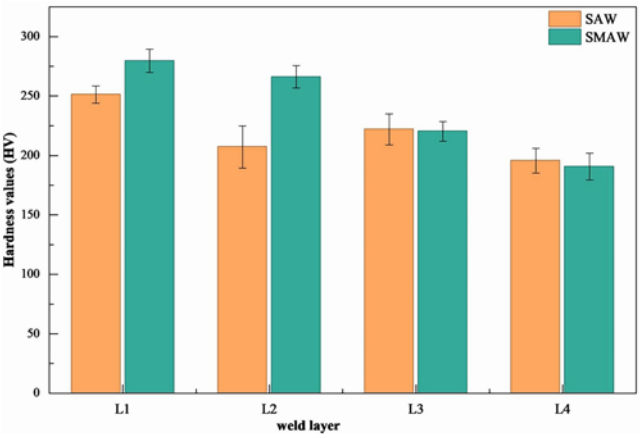


Fig. 14. Average microhardness values of each weld layer in the SMAW and SAW welded joints.

metal, with relatively large differences in average microhardness among the weld layers. In contrast, the SAW weld metal exhibited smaller differences in average microhardness among layers, despite local microhardness fluctuations within individual layers.

The lower heat input of SMAW (9.5–10.5 kJ cm^{-1}), together with its smaller molten pool and faster cooling rate, restricted austenite-grain growth and produced finer columnar grains with smaller dendrite spacing. According to the Hall-Petch strengthening mechanism, grain refinement increases the number of grain boundaries and enhances their resistance to dislocation motion, thereby strengthening the weld metal through grain-boundary strengthening. The EBSD results provide further evidence for the microhardness difference between the two weld metals. The GND densities of the second and third SMAW layers were 0.45×10^{14} and 0.26×10^{14} m^{-2}, respectively, both higher than those of the corresponding SAW layers. A higher GND density indicates larger local orientation gradients and more developed dislocation substructures in the weld metal. These features increase resistance to subsequent plastic deformation and may therefore increase microhardness. Accordingly, the higher overall microhardness of the SMAW weld metal is associated not only with its finer solidification microstructure but also with dislocation and subgrain-boundary strengthening.

In contrast, the higher heat input of SAW (19.6–20.7 kJ cm^{-1}) and longer high-temperature residence time of the molten pool reduced the cooling rate of the weld metal, providing more favorable conditions for austenitic dendrite growth. Consequently, the SAW weld metal developed coarser columnar grains and larger dendrite spacing. The associated grain-boundary strengthening was therefore reduced, resulting in lower overall microhardness than that of the SMAW weld metal. Meanwhile, the small variation in grain-boundary fractions between the second and third SAW layers is consistent with their small difference in average layer microhardness and contributes to improved ductility and toughness. However, the higher heat input also promoted Mn redistribution during solidification. In combination with the EDS and SFE results, the more pronounced dendrite-scale Mn segregation in the SAW weld metal was associated with greater local SFE variations. Consequently, different regions within an individual weld layer experienced distinct local compositional and deformation conditions, leading to variations in local deformation resistance. Therefore, SAW can simultaneously exhibit relatively stable average microhardness among weld layers and pronounced local microhardness fluctuations within an individual layer.

In summary, the microhardness distribution of the weld metals was jointly governed by dendrite size, welding thermal cycles, and Mn segregation. Grain and dendrite sizes, together with dislocation substructures, were associated with overall microhardness level, whereas welding thermal cycles contributed to interlayer differences. Mn segregation and the associated SFE variations may contribute to local microhardness fluctuations. Consequently, SMAW exhibited higher overall microhardness with more pronounced interlayer differences, whereas SAW showed lower overall microhardness and more similar average microhardness among layers but greater intralayer microhardness fluctuations.

3.5.4. Relationship among microstructure, segregation, and mechanical properties

In summary, SMAW and SAW first produce austenitic microstructures with different characteristic sizes through their distinct heat inputs and solidification times. Subsequent multilayer welding thermal cycles then generate differences in Mn distribution, crystallographic characteristics, and mechanical properties. Because both weld metals retain a γ-austenitic matrix, the differences in strength, ductility, cryogenic toughness, and microhardness primarily arise from the coupled effects of grain size, GND density, grain-boundary characteristics, Mn segregation, and local SFE.

For SMAW, the lower heat input and faster cooling rate resulted in relatively refined austenite grains, while the higher GND density further increased resistance to dislocation motion. Consequently, SMAW exhibited higher ultimate tensile strength and overall microhardness. Although its Mn segregation index was lower and its SFE range was narrower, more pronounced variations in grain size, GND density, and grain-boundary fractions were observed between the second and third layers. This indicates that weaker dendrite-scale chemical fluctuations do not necessar-

ily correspond to smaller interlayer crystallographic differences. Such interlayer heterogeneity may limit macroscopic plastic-deformation compatibility, leading to lower elongation after fracture and absorbed impact energy at –196 ℃ than those of SAW.

For SAW, the higher heat input promoted the sufficient growth of columnar grains, with average grain sizes of 151.33 μm and 153.92 μm in the second and third layers, respectively. Together with the lower GND density, this resulted in lower overall microhardness than that of SMAW. Meanwhile, the similar average grain sizes and LAGB/HAGB fractions of the second and third SAW layers favored the maintenance of interlayer deformation continuity. Although the Mn segregation index reached 33.80 % and the local SFE range was wider, all analyzed regions remained within the range favorable for TWIP. Consequently, SAW achieved higher elongation after fracture and cryogenic absorbed impact energy, while the stronger dendrite-scale Mn/SFE fluctuations caused greater microhardness scatter within an individual weld layer.

Accordingly, the relationship among weld microstructure, Mn segregation, and mechanical properties under the two welding processes can be summarized as follows. The rapid solidification during SMAW suppresses Mn diffusion and redistribution and refines the microstructure, resulting in smaller Mn fluctuations and SFE variations, higher GND density, and higher strength and microhardness; however, it also produces more pronounced interlayer microstructural variations. In contrast, the slower solidification during SAW promotes Mn enrichment in interdendritic regions and coarsens the columnar grains, leading to larger Mn/SFE variations and lower microhardness. Nevertheless, the more stable grain-boundary characteristics between the second and third layers and the lower GND density favor improved overall ductility and cryogenic toughness. These results show that similarities between adjacent weld layers can coexist with dendrite-scale chemical heterogeneity. Both scales should therefore be considered when interpreting the strength-toughness balance of high-Mn steel welds.

4. Conclusions

For 20 mm-thick Q400GMDR high-Mn austenitic steel, multilayer multipass welds were produced using shielded metal arc welding (SMAW) and submerged arc welding (SAW). The Mn segregation behavior and its effects on weld microstructure and mechanical properties were investigated under the two welding processes. The main conclusions are as follows:

(1) Both weld metals were predominantly composed of γ-austenite. SMAW produced relatively refined columnar dendrites with more dispersed growth orientations, with average grain sizes of 124.74 μm and 144.29 μm in the second and third layers, respectively. SAW produced coarser columnar grains with stronger growth orientation, with corresponding average grain sizes of 151.33 and 153.92 μm.

(2) The GND densities of the second and third SMAW layers were 0.45×10^{14} and 0.26×10^{14} m^{-2}, respectively, and the corresponding LAGB fractions were 66.4 and 46.2 %, indicating pronounced interlayer crystallographic variations. For SAW, the corresponding GND densities were 0.28×10^{14} and 0.19×10^{14} m^{-2}, and the LAGB fractions were 44.6 and 43.9 %, indicating more similar grain sizes and grain-boundary characteristics between the second and third layers.

(3) Interdendritic Mn enrichment occurred in both weld metals. In SMAW, the local Mn content ranged from 20.63 to 23.39 wt.%, with a segregation index of approximately 12.54 % and an SFE range of 24.0–30.5 mJ m^{-2}. In SAW, the local Mn content ranged from 20.43 to 28.74 wt.%, with a segregation index of approximately 33.80 % and an SFE range of 21.6–33.7 mJ m^{-2}. Both weld metals remained within the SFE range favorable for TWIP; however, SAW exhibited greater dendrite-scale fluctuations in Mn content and SFE.

(4) The finer grains/dendrites and higher GND density in SMAW corresponded to its higher ultimate tensile strength and overall microhardness. In contrast, the lower GND density and more stable grain-boundary characteristics between the second and third SAW layers promoted interlayer plastic-deformation compatibility, resulting in higher elongation after fracture and absorbed impact energy at –196 ℃. The average impact energy at the weld center increased from 68 J for SMAW to 91 J for SAW.

(5) The two processes generated distinct strengthening mechanisms. SMAW was primarily strengthened by microstructural refinement and dislocation substructures, exhibiting smaller local Mn/SFE fluctuations but larger interlayer crystallographic variations. SAW exhibited higher ductility and cryogenic toughness, consistent with more similar microstructural characteristics between the two intermediate layers; its stronger Mn segregation was associated with larger local SFE variations and intralayer microhardness fluctuations.

Acknowledgements

This work was supported by the National Natural Science Foundation of China (Grant No. 52105351), Natural Science Foundation of the Higher Education Institutions of Jiangsu Province (Grant No. 24KJA460002) and the "Shenlan Talent Project" of the Jiangsu University of Science and Technology (No. 2023).

References

[1] M. Choi, J. Lee, H. Nam, N. Kang, M. Kim, D. Cho, Tensile and microstructural characteristics of Fe-24Mn steel welds for cryogenic applications, Met. Mater. Int. 26 (2020) 240–247. https://doi.org/10.1007/s12540-019-00320-4

[2] Q. Luo, H. H. Wang, G. Q. Li, C. Sun, D. H. Li, X. L. Wan, On mechanical properties of novel high-Mn cryogenic steel in terms of SFE and microstructural evolution, Mater. Sci. Eng. A 753 (2019) 91–98. https://doi.org/10.1016/j.msea.2019.02.093

[3] S. Kumar, H.-T. Kwon, K.-H. Choi, J. H. Cho, W. Lim, I. Moon, Current status and future projections of LNG demand and supplies: A global prospective, Energy Policy 39 (2011) 4097–4104. https://doi.org/10.1016/j.enpol.2011.03.067

[4] J.-K. Ren, Q.-Y. Chen, J. Chen, Z.-Y. Liu, On mechanical properties of welded joint in novel high-Mn cryogenic steel in terms of microstructural evolution and solute segregation, Metals 10 (2020) 478. https://doi.org/10.3390/met10040478

[5] J. Kim, J. Kim, C. Pyo, A study on fiber laser welding of high-manganese steel for cryogenic tanks, Processes 8 (2020) 1536. https://doi.org/10.3390/pr8121536

[6] D. Liu, W. Ao, N. Xue, X. Wang, Microstructure and mechanical properties of high manganese steel welded joints for LNG storage tanks using two distinct filler wires, Sci. Technol. Weld. Join. 30 (2025) 327–338. https://doi.org/10.1177/13621718251338351

[7] X. Cai, Y. Qi, H. Zhu, L. Yao, J. Wei, C. Ma, Q. Ge, Cryogenic fracture toughness of high manganese steel joint and 7%Ni steel joint welded with nickel-based filler metal, Mater. Lett. 377 (2024) 137429. https://doi.org/10.1016/j.matlet.2024.137429

[8] H. S. Shin, H. M. Lee, M. S. Kim, Impact tensile behaviors of 9% nickel steel at low temperature, Int. J. Impact Eng. 24 (2000) 571–581. https://doi.org/10.1016/S0734-743X(99)00181-5

[9] M. Bordone, A. Monsalve, J. Perez Ipińa, Fracture toughness of high-manganese steels with TWIP/TRIP effects, Eng. Fract. Mech. 275 (2022) 108837. https://doi.org/10.1016/j.engfracmech.2022.108837

[10] Y.-H. Cho, S.-Y. Park, Y.-K. Kim, J. Kim, J. Han, D.-W. Suh, K.-A. Lee, Fe-36Ni Invar alloy with enhanced strength and low thermal expansion at cryogenic temperatures via laser powder bed fusion, Mater. Sci. Eng. A 949 (2026) 149420. https://doi.org/10.1016/j.msea.2025.149420

[11] B. Wang, Y. Guo, Z. Zhang, X. Yi, D. Wang, Investigation of cryogenic friction and wear properties of Invar 36 alloy against Si3N4 ceramic balls, Wear 518–519 (2023) 204648. https://doi.org/10.1016/j.wear.2023.204648

[12] B. C. De Cooman, Y. Estrin, S. K. Kim, Twinning-induced plasticity (TWIP) steels, Acta Mater. 142 (2018) 283–362. https://doi.org/10.1016/j.actamat.2017.06.046

[13] S. S. Sohn, S. Hong, J. Lee, B.-C. Suh, S.-K. Kim, B.-J. Lee, N. J. Kim, S. Lee, Effects of Mn and Al contents on cryogenic-temperature tensile and Charpy impact properties in four austenitic high-Mn steels, Acta Mater. 100 (2015) 39–52. https://doi.org/10.1016/j.actamat.2015.08.027

[14] Y. Wang, H. Wang, S. Peng, B. Xia, H. Zhu, The dominant role of recrystallization and grain growth behaviors in the simulated welding heat-affected zone of high-Mn steel, Materials 17 (2024) 2218. https://doi.org/10.3390/ma17102218

[15] D. Liu, G. Lv, H. Xiao, Y. Hu, H. Jiao, L. Zhao, D. Chen, Effects of CoCrNi-based fillers on the mechanical properties of high-manganese steel welded joints at room and cryogenic temperatures, Mater. Sci. Eng. A 971 (2026) 150552. https://doi.org/10.1016/j.msea.2026.150552

[16] M. Park, M. S. Kang, G.-W. Park, E. Y. Choi, H.-C. Kim, H.-S. Moon, J. B. Jeon, H. Kim, S.-H. Kwon, B. J. Kim, The effects of recrystallization on strength and impact toughness of cold-worked high-Mn austenitic steels, Metals 9 (2019) 948. https://doi.org/10.3390/met9090948

[17] G.-W. Park, H. Jo, M. Park, S. Shin, W.-S. Ko, N. Park, B.-J. Kim, Y.-S. Ahn, J. Jeon, Microstructure and mechanical properties of gas tungsten arc welded high manganese steel sheet, Metals 9 (2019) 1167. https://doi.org/10.3390/met9111167

[18] S. J. Lee, S. Lee, B. C. De Cooman, Mn partitioning during the intercritical annealing of ultrafine-grained 6% Mn transformation-induced plasticity steel, Scr. Mater. 64 (2011) 649–652. https://doi.org/10.1016/j.scriptamat.2010.12.012

[19] J.-H. Kim, W.-C. Jeong, I. Choi, K.-H. Lee, M.-H. Kim, Fatigue performance of hybrid laser arc welded joints with high manganese steel, Int. J. Nav. Archit. Ocean Eng. 17 (2025) 100660. https://doi.org/10.1016/j.ijnaoe.2025.100660

[20] G. Frommeyer, U. Brüx, P. Neumann, Supra-ductile and high-strength manganese-TRIP/TWIP steels for high energy absorption purposes, ISIJ Int. 43 (2003) 438–446. https://doi.org/10.2355/isijinternational.43.438

[21] O. Grässel, L. Krüger, G. Frommeyer, L. W. Meyer, High strength Fe–Mn–(Al, Si) TRIP/TWIP steels: Development, properties, application, Int. J. Plast. 16 (2000) 1391–1409. https://doi.org/10.1016/S0749-6419(00)00015-2

[22] Y. Qu, L. Ba, C. Li, J. Pan, C. Ma, X. Di, Effect of grain size and segregation on the cryogenic toughness mechanism in heat-affected zone of high manganese steel, Mater. Charact. 213 (2024) 114030. https://doi.org/10.1016/j.matchar.2024.114030

[23] W. Song, T. Ingendahl, W. Bleck, Control of strain hardening behavior in high-Mn austenitic steels, Acta Metall. Sin. Engl. Lett. 27 (2014) 546–556. https://doi.org/10.1007/s40195-014-0084-9

[24] Z. Wang, J. Du, W. Wang, Q. Gao, Y. Yang, L. Xu, X. Xiao, C. Zhu, J. Zeng, Evolution of elements microsegregation in Mn–Cr alloyed steel via combination of solidification and homogenization process, Steel Res. Int. 96 (2025) 308–319. https://doi.org/10.1002/srin.202500155

[25] G.-W. Park, M. Park, B. J. Kim, S. Shin, H. C. Kim, I.-W. Park, S. S. Park, J. B. Jeon, Microstructure and mechanical properties of a gas-tungsten-arc-welded Fe-24Mn-3.5Cr-0.4C high manganese steel pipe using a Fe-22Mn-2.34Ni-0.38C welding wire, Mater. Charact. 194 (2022) 112469. https://doi.org/10.1016/j.matchar.2022.112469

[26] X. Zhuo, T. An, C. Ma, L. Li, Effect of manganese content on the impact toughness and corrosion resistance of deposited metals of weathering steel, Mater. Tehnol. 54 (2020) 189–195. https://doi.org/10.17222/mit.2019.108

[27] X. Fan, Y. Li, Y. Qi, X. Cai, Z. Wang, C. Ma, Mechanical properties of cryogenic high manganese steel joints filled with nickel-based materials by SMAW and SAW, Mater. Lett. 304 (2021) 130596. https://doi.org/10.1016/j.matlet.2021.130596

[28] C. Hu, C. He, X. Gan, X. Wan, F. Hu, W. Zhou, H. Wang, K. Wu, Probing the impact of grain interior and grain boundaries on the mechanical behavior of a high-Mn austenitic steel, J. Mater. Res. Technol. 21 (2022) 5098–5110. https://doi.org/10.1016/j.jmrt.2022.11.085

[29] Y. Dong, X. Y. Qi, L.-X. Du, L. Yan, R. D. K. Misra, Effect of welding thermal cycle on microstructural characteristics and toughness in simulated heat affected zone of low-C medium-Mn high strength steel, J. Mater. Eng. Perform. 31 (2022) 2653–2663. https://doi.org/10.1007/s11665-021-06453-1

[30] T.-U. Park, D.-H. Jung, J.-H. Park, J.-H. Kim, I.-W. Han, Changes in the mechanical properties and microstructure of high manganese steel by high heat input welding and general welding processes, J. Weld. Join. 40 (2022) 33–39. https://doi.org/10.5781/JWJ.2022.40.1.4

[31] W. Jo, J. Lee, D. Seong, G. An, Effect of plastic behavior on the fracture behavior of high manganese austenitic steel welded joints under cryogenic temperatures, Eng. Fract. Mech. 345 (2026) 112451. https://doi.org/10.1016/j.engfracmech.2026.112451

[32] O. Bouaziz, N. Guelton, Modelling of TWIP effect on work-hardening, Mater. Sci. Eng. A 319–321 (2001) 246–249. https://doi.org/10.1016/S0921-5093(00)02019-0

[33] D. T. Pierce, J. A. Jiménez, J. Bentley, D. Raabe, C. Oskay, J. E. Wittig, The influence of manganese content on the stacking fault and austenite/ε-martensite interfacial energies in Fe–Mn–(Al–Si) steels investigated by experiment and theory, Acta Mater. 68 (2014) 238–253. https://doi.org/10.1016/j.actamat.2014.01.001

[34] S. Allain, J.-P. Chateau, O. Bouaziz, S. Migot, N. Guelton, Correlations between the calculated stacking fault energy and the plasticity mechanisms in Fe–Mn–C alloys, Mater. Sci. Eng. A 387–389 (2004) 158–162. https://doi.org/10.1016/j.msea.2004.01.059